Article:
Qi, M.-Y., Tan, C.-L., Tang, Z.-R. et al. (2026) Efficient methanol upcycling to ethylene glycol and glycolaldehyde via divergent C−C coupling synthesis. Nature Communications. ISSN: 2041-1723

https://doi.org/10.1038/s41467-026-69656-x

Nature Communications

https://doi.org/10.1038/s41467-026-69656-x

Article in Press

Efficient methanol upcycling to ethylene glycol and glycolaldehyde via divergent C–C coupling synthesis

Received: 3 June 2025

Accepted: 6 February 2026

Cite this article as: Qi, M.-Y., Tan, C.-L., Tang, Z.-R. *et al.* Efficient methanol upcycling to ethylene glycol and glycolaldehyde via divergent C–C coupling synthesis. *Nat Commun* (2026). https://doi.org/10.1038/s41467-026-69656-x

Ming-Yu Qi, Chang-Long Tan, Zi-Rong Tang, Marco Conte, Yugang Sun & Yi-Jun Xu

Efficient methanol upcycling to ethylene glycol and glycolaldehyde via divergent C–C coupling synthesis

Ming-Yu Qi,[1] Chang-Long Tan,[2] Zi-Rong Tang,*[,1,3] Marco Conte,[4] Yugang Sun,*[,5] and Yi-Jun Xu*[,2,3]

[1] School of Materials and Energy, University of Electronic Science and Technology of China, Chengdu 611731, P. R. China
[2] Institute of Fundamental and Frontier Sciences, University of Electronic Science and Technology of China, Chengdu 611731, P. R. China
[3] College of Chemistry, State Key Laboratory of Photocatalysis on Energy and Environment, Fuzhou University, Fuzhou 350116, P. R. China
[4] School of Mathematical and Physical Sciences, University of Sheffield, Sheffield, S3 7HF, UK
[5] Department of Chemistry, Temple University, 1901 North 13th Street, Philadelphia, Pennsylvania 19122, USA
* To whom correspondence should be addressed.
E-mail: zrtang@uestc.edu.cn; ygsun@temple.edu; yjxu@uestc.edu.cn

Abstract

Direct photocatalytic conversion of methanol into high-value multi-carbon chemicals through precisely controlled C–C coupling represents an extremely appealing but challenging goal. Herein, we demonstrate the efficient photoredox-driven dehydrocoupling of methanol into divergent synthesis of ethylene glycol and glycolaldehyde concomitantly with H_2 production by structural regulation of atomically dispersed Ni species. We showcase distinctly different reaction pathway for divergent C–C coupling of methanol over two types of atomically dispersed Ni cocatalyst-decorated CdS quantum dots, namely those with single Ni atoms (Ni_1-CdS/SiO_2) and Ni clusters (Ni_n-CdS/SiO_2). The Ni_1-CdS/SiO_2 generates ethylene glycol with 90% selectivity by a radical homo-coupling pathway, whereas the Ni_n-CdS/SiO_2 achieves 96% selectivity towards glycolaldehyde by a radical addition-elimination pathway. This work not only offers a fascinating nonpetroleum route for the divergent C–C coupling synthesis of ethylene glycol and glycolaldehyde but also underscores the broad vista of modulating non-selective radicals toward selective transformation of methanol into multi-carbon products.

Introduction

Methanol, which can be sourced from diverse carbon resources, including CO_2, natural/shale gas, coal and biomass, functions as a vastly abundant one-carbon (C_1) building block in today's chemical industry[1-6]. Catalytic methanol transformation involves the activation/conversion of methanol into many types of value-added chemicals, in which the construction of C–C bond represents the most fascinating yet challenging reaction[1]. Presently, methanol conversions associated with C–C bond formation are mainly confined to dehydrative oligomerizations, such as industrial methanol-to-gasoline (MTG) and methanol-to-olefin (MTO) processes, which suffer from restricted selectivity towards target products[7-9]. Against the backdrop of escalating interest

in the methanol economy, it is of urgency and great significance to develop alternative routes for the transformation of methanol via controllable C−C coupling with high reaction efficiency and selectivity.

In principle, the transformation of methanol inevitably involves the activation of either its α-C–H or C−O/O−H bond[1,4]. Of note, the preferential activation of C−O/O−H bond in methanol usually brings along value-reduced oxidation products, especially formaldehyde (HCHO) and even CO_2[10-12]. To access two-carbon (C_2) products via C−C coupling, the selective activation of targeted α-C–H bond in methanol is crucial but challenging[13-16]. Recent years have witnessed the application of metal sulfide semiconductors as photocatalysts to selectively activate the inert α-C–H bond in methanol with the O−H bond intact, thus affording high-reactive hydroxymethyl ($\bullet CH_2OH$) radicals for the synthesis of ethylene glycol (EG)[1,17-22]. Nevertheless, these previous catalytic systems not only encounter the trade-off between activity and selectivity, but also fail to produce other value-added C_2 products because of the pervasive difficulty in steering non-selective $\bullet CH_2OH$ radicals toward controllable C−C coupling pathway for divergent synthesis of C_2 feedstocks. In particular, glycolaldehyde (GLD), a highly attractive C_2 chemical with versatile applications[23-26], has usually been synthesized with low activity and selectivity. These unsolved problems stem from the failure to efficiently manipulate the $\bullet CH_2OH$ radical conversion pathway after the preferential activation and cleavage of α-C–H bond in methanol is achieved. In such a scenario, upon overcoming α-C–H bond-breaking event, the precise regulation of activity/selectivity by preferably steering non-selective $\bullet CH_2OH$ radical conversion route presents a brand-new challenge in advancing methanol chemistry and holds great academic significance.

Herein, we report the ensemble of atomically dispersed Ni-decorated CdS quantum dots (QDs) supported on spherical SiO_2 (Ni-CdS/SiO_2) for the tunable, high-performance photochemical C−C coupling of methanol into EG and GLD integrated with concomitant H_2 production at ambient conditions. The present CdS QDs can selectively activate the unreactive α-C–H bond in methanol with the O−H group intact, thus affording sufficient high-reactive $\bullet CH_2OH$ radicals. Loading CdS QDs onto the SiO_2 support not only regulates the dielectric environment of CdS QDs via the near-field scattering promoted optical absorption model for enhanced light-capturing property[15,27,28], but also improves their antiphotocorrosion ability and recyclability. Two types of atomically dispersed Ni species, single Ni atoms for Ni_1-CdS/SiO_2 and Ni clusters for Ni_n-CdS/SiO_2, act as active sites to govern $\bullet CH_2OH$ radicals conversion pathway for precisely tailoring the C−C coupling synthesis between EG and GLD formation reaction, along with significantly enhanced activity. As an outcome, EG is generated with 90% selectivity over the Ni_1-CdS/SiO_2 catalyst, and a high selectivity of 96% towards GLD is obtained over the Ni_n-CdS/SiO_2 catalyst. Mechanistic insights by joint theoretical and experimental studies unveil that the divergent synthesis of EG and GLD over Ni-CdS/SiO_2 originates from the single Ni atoms-assisted homo-coupling of $\bullet CH_2OH$ radicals and Ni clusters-catalyzed radical addition-elimination mechanism, respectively.

Results

Preparation and characterization of Ni-CdS/SiO_2 with atomically dispersed Ni species

The schematic diagram of the fabrication of atomically dispersed Ni-decorated CdS QDs supported on spherical SiO_2 (Ni-CdS/SiO_2) is depicted in **Fig. 1a**. Initially, CdS QDs were prepared

by a one-pot synthesis using 3-mercaptopropionic acid (MPA) as capping molecule (**Supplementary Table 1**), and then loaded onto the SiO_2 support (CdS/SiO_2) through an electrostatic self-assembly strategy. Transmission electron microscopy (TEM) images afford the detailed insights into the microscopic structures and morphologies of CdS/SiO_2 composite. In contrast to the smooth surface of SiO_2 sphere (**Supplementary Fig. 1a** and **b**), the uniform distribution of CdS QDs can be distinctly identified on the surface of SiO_2 sphere within the CdS/SiO_2 composite (**Fig. 1b**). Subsequently, photodeposition of Ni species onto CdS/SiO_2 was performed using $NiCl_2{\cdot}6H_2O$ as the precursor under 0.5 h of xenon-lamp irradiation. The CdS/SiO_2 composite contains abundant dangling –COOH groups originating from MPA, which serve to adsorb and anchor Ni^{2+} cations (**Supplementary Fig. 2**)[28,29]. The Ni-CdS/SiO_2 composites with different Ni loading contents were obtained by regulating the amount of Ni precursor (**Supplementary Table 2**, the two representative samples of $Ni_{0.1}$-CdS/SiO_2 and $Ni_{1.0}$-CdS/SiO_2 with the lowest and highest Ni loading amounts are denoted as Ni_1-CdS/SiO_2 and Ni_n-CdS/SiO_2, respectively). High-resolution TEM (HR-TEM, **Supplementary Fig. 1c** and **d**) analysis exhibits the ordered lattice fringe with a *d*-spacing of 0.335 nm, ascribed to the (111) crystal plane of cubic CdS[28]. No formation of Ni-derived nanoparticles is observed in high-resolution TEM images of both the Ni_1-CdS/SiO_2 and Ni_n-CdS/SiO_2, certifying that the Ni species in these two catalysts are both atomically dispersed on CdS/SiO_2. As illustrated in **Supplementary Fig. 1e**, elemental mapping results further validate the even dispersion of Cd, S and Ni elements throughout the SiO_2 support. From aberration-corrected high-angle annular dark-field scanning TEM (**Supplementary Fig. 3**), high-density bright dots assigned to the overlapped image contrast of Cd atom and Ni atom are observed in Ni_n-CdS/SiO_2, confirming the formation of Ni clusters.

To gain the local coordination structure of Ni species, X-ray absorption spectroscopy (XAS) measurements were performed. **Fig. 1c** shows the Ni K-edge X-ray absorption near-edge structure (XANES) spectra of Ni_1-CdS/SiO_2 and Ni_n-CdS/SiO_2 in reference to Ni foil and NiO. The threshold energy of Ni_1-CdS/SiO_2 falls between Ni foil and NiO, suggesting an electron-deficient state of $Ni^{\delta+}$ ($0 < \delta < 2$)[30,31], and that of Ni_n-CdS/SiO_2 is close to standard NiO, manifesting that the electronic state of Ni species in Ni_n-CdS/SiO_2 is approximate to +2[29,32], consistent with the X-ray photoelectron spectroscopy (XPS) results (**Supplementary Fig. 4** and **5**). As sketched in **Fig. 1d**, the extended X-ray absorption fine structure (EXAFS) spectrum of Ni_1-CdS/SiO_2 only features a prominent peak at 1.38 Å from Ni–O coordination, suggesting the formation of isolated Ni atom in Ni_1-CdS/SiO_2[28,33]. For Ni_n-CdS/SiO_2, an additional peak at about 2.69 Å from Ni–Ni coordination emerges, corroborating the formation of Ni clusters[29]. The trend can also be clearly resolved from the wavelet transform on Ni K-edge EXAFS oscillations (**Fig. 1e**,**f** and **Supplementary Fig. 6**). From the fitting structural parameters (**Fig. 1g**,**h**, **Supplementary Fig. 7** and **Supplementary Table 3**), the Ni-O coordination number in Ni_1-CdS/SiO_2 is evaluated to be 2.6 ± 0.2, indicating the Ni single atoms with a $Ni–O_3$ moiety. In addition, the Ni-O and Ni–Ni coordination numbers of Ni clusters in Ni_n-CdS/SiO_2 are calculated to be 6.4 ± 0.2 and 3.5 ± 0.3, respectively. The above results elucidate that these two catalysts exhibit distinct difference in electronic structure as well as in coordination environment. With the further aid of density functional theory (DFT) optimization calculations, the most stable structures of Ni_1-CdS/SiO_2 and Ni_n-CdS/SiO_2 are sketched in **Supplementary Fig. 8**.

Selective dehydrocoupling of methanol to produce EG or GLD

Subsequently, we evaluated the application of Ni-CdS/SiO_2 for dehydrocoupling of methanol to EG or GLD integrated with H_2 evolution, in one tunable photoredox catalytic system (**Fig. 2a**). As displayed in **Fig. 2b** and **c**, the blank CdS QDs exhibit low EG and H_2 production rates, reaching only 1.9 and 2.8 mmol $g_{Ni\text{-}CdS}^{-1}$ h^{-1}, respectively. Compared to bare CdS QDs, CdS/SiO_2 presents much higher EG formation rate of 4.1 mmol $g_{Ni\text{-}CdS}^{-1}$ h^{-1}; meanwhile, the production rate of H_2 improves from 2.8 to 6.4 mmol $g_{Ni\text{-}CdS}^{-1}$ h^{-1}, which is attributed to the distinctly enhanced optical absorption correlated to the scattering resonances of the SiO_2 supports (**Supplementary Fig. 9**)[15,28]. Upon decorating with Ni, the Ni_1-CdS/SiO_2 exhibits significantly enhanced EG formation rate (16.8 mmol $g_{Ni\text{-}CdS}^{-1}$ h^{-1}) by 3.1 times as compared to CdS/SiO_2, along with a high EG selectivity of 90% (**Supplementary Fig. 10-14**). Remarkably, as the Ni loading increases, the selective product in the dehydrocoupling of methanol transitions from EG to GLD (**Supplementary Fig. 10-14**). Consequently, over Ni_n-CdS/SiO_2, a GLD evolution rate of 24.1 mmol $g_{Ni\text{-}CdS}^{-1}$ h^{-1} is achieved with 96% selectivity (**Fig. 2b**). In addition, the production of H_2 increases along with Ni loading amount, and the ratios of electrons (consumed for the reduction product H_2) to holes (consumed for the oxidation products EG/GLD/HCHO) over different catalysts are calculated to be approximately 1:1 (**Supplementary Table 4**), indicating a stoichiometric dehydrocoupling reaction. It is noteworthy that HCHO (a major by-product of methanol oxidation) consistently maintains an exceedingly low evolution rate (< 1.2 mmol $g_{Ni\text{-}CdS}^{-1}$ h^{-1}) in the current catalysis system. In addition, the optimized apparent quantum yields (AQYs) of 12.3% for EG and 17.2% for GLD are attained over Ni_1-CdS/SiO_2 and Ni_n-CdS/SiO_2 respectively, at λ = 370 nm (**Fig. 2d** and **Supplementary Table 5**). Compared with previously reported catalytic systems (**Supplementary Table 6**)[1,17-22], this work highlights the realization of photocatalytic methanol coupling for the divergent synthesis of EG and GLD concomitantly with H_2 production.

The stability of Ni-CdS/SiO_2 was then investigated by cycle experiments, as shown in **Fig. 2e** and **f**. After five repeated tests of totaling 50 h, the catalytic performance for EG (or GLD) and H_2 coproduction over Ni_1-CdS/SiO_2 (or Ni_n-CdS/SiO_2) remains relatively stable; nevertheless, that of unsupported CdS QDs decreases by 42.8% for EG and 43.6% for H_2 (**Supplementary Fig. 15**). The high-resolution XPS analysis in **Supplementary Fig. 16** illustrates the good maintenance of element composition in used Ni_1-CdS/SiO_2 compared with fresh Ni_1-CdS/SiO_2. In addition, element leakage after 10 h of continuous light irradiation was evaluated. As shown in **Supplementary Table 7**, only slight Cd^{2+} leakages of 1.34 μg and 1.12 μg are observed in Ni_1-CdS/SiO_2 and Ni_n-CdS/SiO_2 respectively, which are much lower than those of bare CdS QDs (7.35 μg for Cd^{2+}). These results collectively illustrate that this self-assembly strategy suppresses the photocorrosion of CdS QDs and facilitates the recovery of CdS QDs from the reaction solvent. Furthermore, taking into account that single atoms may aggregate under light irradiation[34,35], we performed additional XAS characterizations on Ni_1-CdS/SiO_2 after five consecutive reaction cycles. Notably, in the EXAFS spectrum of the used Ni_1-CdS/SiO_2 after 50 h of light exposure, an additional weak peak emerges at approximately 2.64 Å from Ni–Ni coordination (**Supplementary Fig. 17**), indicating the partial agglomeration of single Ni atoms during the prolonged light irradiation (**Supplementary Table 8**), which accounts for the slight decrease in EG selectivity (**Fig. 2e**).

Mechanism insight for dehydrocoupling of methanol

Given that the charge separation dynamics usually restricts the catalytic performance, photo-electrochemical characterizations were first carried out. As depicted in **Supplementary Fig. 18a**, the transient photocurrent densities of these samples increase in the following sequence: CdS/SiO_2 < Ni_1-CdS/SiO_2 < Ni_n-CdS/SiO_2, implying that decorating CdS/SiO_2 with Ni species remarkably enhances the charge separation efficiency, which was further verified by the electrochemical impedance spectroscopy (EIS) analysis (**Supplementary Fig. 18b**). These results distinctly indicate that the incorporation of atomically dispersed Ni species into CdS/SiO_2 facilitates the conversion of methanol to EG or GLD for a significantly boosted activity by expediting the separation and transfer of photogenerated electrons and holes.

To probe the reaction mechanism of methanol coupling to EG/GLD integrated with H_2 evolution in the present catalytic system, the band structure of CdS QDs was measured. As displayed in **Fig. 3a**, Tauc plot indicates the bandgap energy (E_g) of CdS QDs to be around 2.48 eV. The conduction-band (CB) edge of CdS QDs is measured with the value of −0.72 V vs NHE based on the Mott–Schottky curve, and the valence-band (VB) edge of CdS QDs is thus calculated to be 1.76 V vs NHE. Taking into account both the limited interfacial contact between Ni species and CdS QDs enabled by the capping molecule of MPA and the low Ni loading amount (0.1 to 1%)[36-38], anchoring Ni species is insufficient to induce significant alterations to the band structure of CdS QDs. In addition, the redox potential of methanol is evaluated at about 0.61 V vs NHE by virtue of the cyclic voltammograms (**Supplementary Fig. 19**)[39-41]. Obviously, the CB edge of CdS QDs is higher than $E(H^+/H_2)$ (−0.41 V vs. NHE), and the VB edge is lower than E(methanol/methanol$^{\bullet+}$), which fulfills the thermodynamic constraints for the synchronous occurrence of these two half-reactions (**Fig. 3b**)[11].

To further decipher the function-oriented effects of Ni decoration with regard to the selectivity regulation in methanol coupling to EG and GLD, we performed a set of control experiments. As shown in **Supplementary Fig. 20**, the catalytic performance (including EG, GLD and H_2 production rates as well as EG/GLD selectivity) of both $Ni_{1\text{-}IM}$-CdS/SiO_2 and $Ni_{n\text{-}IM}$-CdS/SiO_2 synthesized through impregnation method is significantly lower than that of the corresponding Ni_1-CdS/SiO_2 and Ni_n-CdS/SiO_2, suggesting the structural advantages of atomically dispersed Ni species afforded by the photodeposition strategy. In the absence of catalyst or light, the photocatalytic reaction cannot proceed at all (**Fig. 3c** and **d**). The introduction of CCl_4 as an electron scavenger almost terminates the H_2 production, and moreover, the generation of EG or GLD is decelerated considerably once adding triethanolamine (TEOA) as a hole scavenger, indicating the joint participation of photogenerated electrons and holes in the evolution of H_2 and EG/GLD. In addition, comparative reaction with EG employed as the reactant was performed to investigate the possible consecutive oxidation of EG. Notably, no product is detected over both Ni_1-CdS/SiO_2 and Ni_n-CdS/SiO_2 during the experimental process, which suggests that EG can exist stably and GLD is not originated from the overoxidation of EG. Furthermore, the time-dependent product distributions for the dehydrocoupling of methanol illustrate that the production of EG over Ni_1-CdS/SiO_2 increases as the reaction time extends (**Fig. 3e**). An induction period is clearly observed, since stabilizing both the adsorption-desorption equilibrium of reactants (i.e., methanol molecules) on the catalyst surface and the accumulation of initial reaction intermediates demands a short duration. Meanwhile, the yields of GLD and HCHO exhibit an upward trend, albeit with extremely low values during the reaction process. In contrast, although HCHO also

maintains a relatively low output over Ni_n-CdS/SiO_2, its generation presents a trend of first increasing and then decreasing with the reaction proceeding (**Fig. 3f**), which indicates that in this catalytic system, HCHO is not a by-product but an intermediate for the production of target product GLD.

To gain further insights, in-situ electron paramagnetic resonance (EPR) spectroscopic studies were adopted to monitor the radical intermediates involved in the dehydrocoupling of methanol using 5,5-dimethyl-1-pyrroline *N*-oxide (DMPO) as a spin-trapping reagent (**Fig. 3g**). Under light irradiation, the generated •CH_2OH radical is trapped by DMPO, as manifested by the characteristic peaks belonging to the DMPO-CH_2OH adduct[1]. Upon Ni decoration, an obvious increase in the evolution rate of •CH_2OH radical is observed over Ni_1-CdS/SiO_2 and Ni_n-CdS/SiO_2, indicating that Ni species significantly promotes the cleavage of α-C−H bond in methanol. It is noted that the methoxyl (CH_3O•) radical, commonly generated in the conversion of methanol[1,17], is absent in the EPR spectra, which is maybe due to the small amount of CH_3O• radical generated in this catalytic system as well as its short-lived nature[1]. In addition, through the in-situ capture of •CH_2OH radical by 1,1-diphenylethylene (DPE)[18], the product of 3,3-diphenylpropan-1-ol (DPE-CH_2OH) is obtained over Ni_1-CdS/SiO_2, with a selectivity of 95% according to the gas chromatography results (**Fig. 3h**, **Supplementary Fig. 21** and **22**). Another trace product of 3-methoxy-3,3-diphenylpropan-1-ol (CH_3O-DPE-CH_2OH) is attributed to the addition of methoxy radical (CH_3O•) to DPE-CH_2OH. These findings illustrate that the preferential cleavage of α-C−H bond to generate •CH_2OH radical in methanol than the O−H bond occurs readily on Ni_1-CdS/SiO_2, thereby generating EG via •CH_2OH radical coupling[1,18]. By contrast, for the case over Ni_n-CdS/SiO_2, capturing radicals by DPE affords the products of DPE-CH_2OH and CH_3O-DPE-CH_2OH with selectivities of 79% and 21%, respectively—corresponding to the radical selectivities of 83% for •CH_2OH radical and 17% for CH_3O• radical, indicating that the cleavage of both α-C−H and O−H bond in methanol occurs concurrently on Ni_n-CdS/SiO_2. This distinctly enhanced generation of CH_3O• radical originating from O−H cleavage of methanol is answerable for the formation of HCHO intermediate[42]. As corroborated by the dynamic trend of HCHO yield (first increasing and then decreasing) observed in **Fig. 3f**, the as-generated HCHO intermediate subsequently reacts with the •CH_2OH radical to afford GLD via the Ni clusters-assisted addition-elimination mechanism, as further confirmed by our theoretical calculations below.

Upon gathering the above results, DFT calculations were further carried out to shed light on the selectivity regulation between EG and GLD synthesis and the overall reaction pathways for the dehydrocoupling of methanol over Ni_1-CdS/SiO_2 and Ni_n-CdS/SiO_2. Based on the EXAFS analysis, single Ni atoms and Ni clusters coordinated with the capping molecule of MPA on the surface of CdS QDs are selected to represent the catalytic sites on Ni_1-CdS/SiO_2 and Ni_n-CdS/SiO_2, respectively. To establish reliable reaction energy profiles, we first screened various plausible adsorption configurations and then adopted the most stable geometries for subsequent calculations (**Supplementary Fig. 23-28**). As sketched in **Fig. 4a**, both methanol adsorption steps over Ni_1-CdS/SiO_2 and Ni_n-CdS/SiO_2 composite are thermodynamically downhill with the values of −0.056 and −0.453 eV, respectively. For the Ni single atom-assisted catalytic mechanism, the first deprotonation step of methanol over Ni_1-CdS/SiO_2 is endergonic to afford •CH_2OH radical via overcoming the relative energy of 0.494 eV. Subsequently, a homo-coupling pathway for EG production is thermodynamically favorable (0.015 eV) compared with the addition-elimination

mechanism for GLD production (0.702 eV) or the second deprotonation route for HCHO production (1.135 eV). Under the catalytic mechanism supported by the Ni cluster, the homo-coupling of •CH_2OH radical is exothermic with the values of −0.368 eV; nevertheless, the desorption step of EG is considerably more difficult owing to the high relative energy of 1.095 eV. On the contrary, a thermodynamically more feasible reaction pathway is that, the •CH_2OH radical undergoes an addition-elimination pathway with a negligible condensation energy of 0.090 eV, followed by an exergonic deprotonation to produce GLD (−0.539 eV). The desorption process of GLD is regarded as the rate-limiting step by overcoming a moderate relative energy of 0.633 eV. Although DFT has inherent limitations in modeling specific materials under realistic catalytic conditions, the conclusions drawn from DFT are helpful to understand the role of Ni atoms and Ni clusters in regulating selectivity between EG and GLD synthesis. Taking the above theoretical and experimental results into account together, the overall catalytic reaction mechanism for highly selective and divergent synthesis of EG and GLD over Ni_1-CdS/SiO_2 with single Ni atoms and Ni_n-CdS/SiO_2 with Ni clusters is put forward correspondingly, as displayed in **Fig. 4b**.

Discussion

In summary, we report the efficient photoredox-catalyzed dehydrocoupling of methanol into tunable EG by a radical homo-coupling pathway and GLD by a radical addition-elimination pathway over the different atomically dispersed Ni-decorated CdS/SiO_2 composite under ambient conditions. EG (90% selectivity) and GLD (96% selectivity) are preferentially generated over Ni_1-CdS/SiO_2 with single Ni atoms and Ni_n-CdS/SiO_2 with Ni clusters, respectively, along with competitive reactivity compared with other catalytic systems. Mechanistic insights into the divergent synthesis of EG and GLD are proposed based on joint experimental results and DFT calculations. The structure-performance relationship established over atomically dispersed Ni cocatalysts advances our understanding of catalyst design for methanol conversion, paving the way for future progress in devising catalysts for efficient and divergent synthesis of sustainable chemicals.

Methods

Chemicals and materials. Sodium sulfide nonahydrate ($Na_2S·9H_2O$, >98%), cadmium chloride hemipentahydrate ($CdCl_2·2.5H_2O$, >99%), sodium hydroxide (NaOH, >96%), tetraethyl orthosilicate ($C_8H_{20}O_4Si$, TEOS, >99%), isopropanol (C_3H_8O, >99.7%), ammonium hydroxide ($NH_3·H_2O$, 25%), acetonitrile (CH_3CN, >99.9%), anhydrous ethanol (C_2H_6O, >99.5%), nickel chloride hexahydrate ($NiCl_2·6H_2O$, >98%) and 5,5-dimethyl-1-pyrroline *N*-oxide ($C_6H_{11}NO$, DMPO, >97%) were supplied by Sinopharm chemical reagent Co., Ltd. (Shanghai, China). Methanol (CH_3OH, >99.8%), ethylene glycol ($C_2H_6O_2$, >99.8%), glycolaldehyde ($C_2H_4O_2$, >99%), 1,1-diphenylethylene ($C_{14}H_{12}$, >97%), acetylacetone ($C_5H_8O_2$, >99.5%) and ammonium acetate ($C_2H_7NO_2$) were obtained from Aladdin Biochemical Technology Co. Ltd. (Shanghai, China). 3-mercaptopropionic acid ($C_3H_6O_2S$, MPA, >98%) and branched poly-ethylenimine (M_w = 25000, BPEI) were purchased from Sigma-Aldrich. All materials were used as received without further treatment. Deionized water was obtained from local sources.

Synthesis of CdS QDs. Generally, 1 mmol of $CdCl_2·2.5H_2O$ and 1.7 mmol of MPA were added in 20 mL of deionized water, with the solution pH tuned to nearly 10 by dropwise addition of NaOH solution. The resulting mixture was transferred to a three-necked flask, which was then purged

with Ar gas. Under magnetic agitation, 5 mL of 0.2 M Na_2S solution was rapidly injected into the flask. The reaction mixture was then heated to 100 °C under reflux with a condenser attached, and the bright-yellow solution was agitated for 0.5 h at 100 °C to facilitate the growth of CdS QDs. After cooling to room temperature, the as-synthesized product was collected via precipitation with the addition of ethanol, and subsequently dried in an oven.

Synthesis and functionalization of SiO_2 spheres. Generally, 2 mL of TEOS was introduced into a mixed solution containing 40 mL of isopropanol, 1 mL of deionized water and 2 mL of 10.5 M $NH_3 \cdot H_2O$ under continuous magnetic agitation. Following 6 h of reaction, the formed suspensions were isolated via centrifugation at 5000 rpm and rinsed alternately with ethanol and deionized water for several times. The resulting SiO_2 spheres were dried in an oven at 60 °C. For the positive charge functionalization of SiO_2 surfaces, 0.4 g of SiO_2 spheres were ultrasonically dispersed in 200 mL of ethanol, and 344 mg of BPEI was subsequently added to the dispersion. The resultant mixture was heated to 60 °C under oil bath conditions for 6 h. Thereafter, the obtained product was thoroughly rinsed with ethanol and deionized water to eliminate unreacted BPEI residues, and finally dried in an oven.

Synthesis of CdS/SiO_2 composites. Initially, 0.2 g of BPEI-SiO_2 was ultrasonically dispersed in 200 mL of deionized water. Next, 10 mg of CdS QDs were introduced to the above dispersion, and the resultant mixture was refluxed in an oil bath at 60 °C. Thereafter, the as-prepared CdS/SiO_2 composites were isolated by centrifugation, rinsed repeatedly with deionized water, and then dried in an oven. The actual loading content of CdS QDs in CdS/SiO_2 composites is 5 wt%.

Synthesis of Ni-CdS/SiO_2 composites. Generally, 50 mg of CdS/SiO_2 was dispersed in 50 mL of water/ethanol (40/10 mL) mixed solution containing $NiCl_2 \cdot 6H_2O$ (17.04 μmol mL^{-1}, equivalent to 1 mg_{Ni} mL^{-1}, 50 μL, 100 μL, 250 μL and 500 μL). The resulting suspension was then irradiated with a 300 W xenon lamp (PLS-SXE 300D, Beijing Perfectlight Co., Ltd.) for 0.5 h under N_2 atmosphere. The resulting products were collected by centrifugation and rinsed with deionized water. Finally, the Ni-CdS/SiO_2 composites with different Ni weight loadings (0.1%, 0.2%, 0.5% and 1.0%) were obtained.

Synthesis of Ni_{IM}-CdS/SiO_2 composites. Generally, 50 mg of CdS/SiO_2 was dispersed in 50 mL of water/ethanol (40/10 mL) mixed solution containing $NiCl_2 \cdot 6H_2O$ (17.04 μmol mL^{-1}, 50 μL and 500 μL). The resulting suspension was then evaporated using a rotary evaporator in a 60 °C water bath. After further drying in an oven at 60 °C, Ni_{IM}-CdS/SiO_2 composites with different Ni weight loadings (0.1% and 1.0%), designated as $Ni_{1\text{-}IM}$-CdS/SiO_2 and $Ni_{n\text{-}IM}$-CdS/SiO_2, were obtained.

Characterization. X-ray photoelectron spectroscopy (XPS) was conducted on a Thermo Scientific ESCA Lab250 spectrometer, with all binding energies calibrated against the C 1s peak at 284.8 eV. The morphology features and elemental distribution of the samples were investigated via transmission electron microscopy (TEM) and energy dispersive X-ray spectroscopy (EDX) on a JEOL model JEM 2010 EX microscope. Aberration-corrected high-angle annular dark-field scanning TEM (HAADF-STEM) was carried out on a FEI Themis Z field emission transmission electron microscope (Titan Cubed Themis G2300, JEM-ARM200F). UV-vis diffuse reflectance spectroscopy (DRS) was performed using a Thermo Scientific Evolution 200 Series UV-vis spectrophotometer to determine the optical properties of the samples. Electron paramagnetic resonance (EPR) measurements were conducted on a Bruker A300 EPR spectrometer. For in situ EPR tests, 20 mg of sample was ultrasonically dispersed in 10 mL of methanol containing 0.2

mmol of DMPO. The resulting suspension was then injected into a glass capillary, which was placed in a sealed glass tube under Ar atmosphere. This sealed glass tube was positioned in the microwave cavity of the EPR spectrometer, and irradiated with a 300 W xenon lamp during EPR tests at room temperature. The contents of Cd, S and Ni were quantified via inductively coupled plasma-mass spectrometry (ICP-MS, PerkinElmer NexION 300X). X-ray absorption spectra were collected at beamline BL01C1 of NSRRC. The radiation was monochromatized using a Si (111) double-crystal monochromator, and all measurements were carried out in fluorescence mode. A Pt foil was placed downstream of the sample cell to serve as a reference for calibrating the photon energy of each spectrum. The raw spectral data were subjected to Pt foil-based energy calibration, background correction, normalization and fitting processes using the ATHENA and ARTEMIS software packages.

Electrochemical/photoelectrochemical measurements. Electrochemical measurements were performed in a three-electrode system, where a Pt plate served as the counter electrode and an Ag/AgCl electrode was used as the reference electrode. The working electrode was fabricated on fluorine-doped tin oxide (FTO) glass, and the edges of the FTO substrate were masked with Scotch tape to restrict the exposed area to 0.25 cm^2. For electrode preparation, 5 mg of sample was dispersed in a mixed solution containing 1 mL of N,N-dimethylformamide and 50 µL of Nafion solution. 25 µL of this slurry was uniformly coated onto the pretreated FTO glass. After being dried at 60 °C, the uncoated parts of the electrode were insulated with epoxy resin. Photocurrent density was tested using an Autolab M204 electrochemical workstation in 0.2 mol L^{-1} Na_2SO_3 solution, with irradiation provided by a 300 W xenon lamp. Both Mott-Schottky analysis and electrochemical impedance spectroscopy were carried out in 0.5 mol L^{-1} of KCl solution supplemented with 0.01 mol L^{-1} of $K_3[Fe(CN)_6]/K_4[Fe(CN)_6]$. Cyclic voltammetry (CV) was also conducted on the Autolab M204 workstation. The electrolyte was prepared by adding 1 mol L^{-1} of methanol and 0.1 mol L^{-1} of tetrabutylammonium hexafluorophosphate (as the supporting electrolyte) to acetonitrile. Before the tests, the electrolyte solution was degassed by purging with N_2 gas, and the CV scans were performed at 100 mV s^{-1}. All potential values were recorded relative to the normal hydrogen electrode (NHE).

Photoactivity testing. Selective dehydrocoupling of methanol to EG or GLD integrated with H_2 generation was conducted in a double-walled quartz reactor, maintained at 25 °C via circulating water flow. Typically, 20 mg of sample was added into 10 mL of methanol, which was then purged with Ar gas for 15 min. Subsequently, a 300 W xenon lamp (PLS-SXE 300D) served as the light source, with its light power density reaching around 0.18 W cm^{-2}. The evolved H_2 was quantitatively determined using a gas chromatograph (Shimadzu GC-8A 2014C), and the evolved EG and GLD were determined by gas chromatography-mass spectrometry (Shimadzu GC-MS QP2020). In addition, the by-product of HCHO was quantified by the acetylacetone colorimetric determination method. For the assessment of the catalyst's photocatalytic stability, five consecutive recycling experiments were performed, with the detailed experimental protocol described as follows. Following the first photocatalytic reaction cycle, the catalyst was recovered by centrifugation, rinsed twice with methanol, and then dried in an oven. Thereafter, the second cycle was conducted by re-dispersing the recovered catalyst into fresh methanol solution, and the rest of the cycles followed the same protocol.

Determination of HCHO. The amount of HCHO product was quantified by acetylacetone colorimetric method. The preparation of 0.25% (v/v) acetylacetone solution was as follows: 25 g of ammonium acetate was dissolved in 50 mL of deionized water, 3 mL of acetic acid and 0.25 mL of acetylacetone were then added in sequence. Afterwards, the solution was transferred to 100 mL volumetric flask and diluted with water to 100 mL. Specifically, 2.4 mL of the liquid product supernatant after reaction was mixed with 1.6 mL of the as-prepared acetylacetone solution in a glass bottle, which was heated for 3 min in 100 °C oil bath, then the colorless solution could turn into the yellow color. Afterwards, a specific amount of liquid was taken out to measure the UV-vis absorption spectrum. Through the absorbance intensity at 402 nm, the HCHO amount was achieved by referenced to standard curve.

Determination of generation rates and apparent quantum yield (AQY). The generation rates of EG, GLD and H_2 were calculated according to the following equation:

$$\text{Generation rates} = \frac{n_{products}}{m_{catalyst} \times t} \quad (1)$$

where n is the molar amount of the obtained products (EG, GLD and H_2), m is the mass of catalyst (normalized based on the mass of Ni-CdS), and t is the reaction time.

The AQYs of EG and GLD for the Ni_1-CdS/SiO_2 and Ni_n-CdS/SiO_2 were measured using incident light through different wavelength band-pass filters (370, 430, 450, 510, 650 and 750 nm). Photon flux of the incident light was measured with a PL-MW200 photoradiometer (Beijing Perfectlight Co., Ltd.). The AQY was calculated using the following equation:

$$\text{AQY} = \frac{N_h}{N_p} \times 100\% = \frac{n \times M \times \mathrm{N_A} \times \mathrm{h} \times \mathrm{c}}{S \times P \times t \times \lambda} \times 100\% \quad (2)$$

where N_h and N_p denote the number of reaction holes and incident photons, n represents the number of holes consumed per molecule of EG (n = 2) or GLD (n = 4) generated, M refers to the molar amount of EG or GLD, N_A denotes the Avogadro constant, h represents the Planck constant, c is the speed of light, S refers to the irradiation area, P denotes the light power density, t stands for the reaction time and λ represents the wavelength of the incident light. A representative calculation procedure is presented in **Supplementary Table 5**.

Computational details. First-principles DFT calculations were carried out with the Vienna Ab initio Simulation Package (VASP) by employing the projector-augmented-wave (PAW) method[43]. The exchange-correlation functional was adopted within the framework of the generalized gradient approximation (GGA) for the Perdew-Burke-Emzerhof (PBE) functional[44]. Spin polarization was employed in all computational processes. An energy cutoff of 450 eV was assigned to the plane wave basis set, and a convergence criterion of 0.05 eV/Å for the maximum residual force on each atom was applied for geometric relaxation. The Brillouin zone was sampled using the surfaces structures of 2 × 2 × 1 Monkhorst-Pack K-point mesh. Self-consistent calculations were conducted with an energy convergence threshold of 10^{-5} eV. The DFT-D3 method was adopted to account for van der Waals interactions, and a 15 Å vacuum layer was introduced along the z-axis to eliminate the interactions between periodic structures. Furthermore, the lattice parameters of the two models were kept identical, with a = b = 16.803 Å, c = 33.182 Å, α = β = 90°, and γ = 120°. Structural relaxation calculations were performed for all structures, and the convergence criteria for energy and force mentioned earlier were satisfied.

During the optimization process, the bottom two atomic layers were fixed to simulate the properties of the bulk phase, while all remaining atoms were allowed to relax freely. The free energies of the reaction steps were calculated by the equation:

$$\Delta G = \Delta E_{DFT} + \Delta E_{ZPE} - T\Delta S \quad (3)$$

where ΔE_{DFT} represents the DFT-calculated electronic energy difference for each reaction step, ΔE_{ZPE} and ΔS refer to the zero-point energy (ZPE) correction and entropy change, respectively, which are derived from vibration analysis, T denotes the temperature, which is set at 300 K. The details of DFT models, ZPE correction and entropy values are supplemented in **Supplementary Table 9** and **Supplementary Data 1**.

Data availability

The authors declare that all data supporting the findings of this study are available in the article and its Supplementary Information. Source data are provided as a Source Data file. Source data are provided with this paper.

References

1 Xie, S. *et al.* Visible light-driven C-H activation and C-C coupling of methanol into ethylene glycol. *Nat. Commun.* **9**, 1181 (2018).

2 Jiao, J. *et al.* Sun-simulated-driven production of high-purity methanol from carbon dioxide. *Nat. Commun.* **16**, 857 (2025).

3 Yang, H. *et al.* Potential-driven structural distortion in cobalt phthalocyanine for electrocatalytic CO_2/CO reduction towards methanol. *Nat. Commun.* **15**, 7703 (2024).

4 Moran, J., Preetz, A., Mesch, R. A. & Krische, M. J. Iridium-catalysed direct C-C coupling of methanol and allenes. *Nat. Chem.* **3**, 287-290 (2011).

5 Graciani, J. *et al.* Highly active copper-ceria and copper-ceria-titania catalysts for methanol synthesis from CO_2. *Science* **345**, 546-550 (2014).

6 Dummer, N. F. *et al.* Methane Oxidation to Methanol. *Chem. Rev.* **123**, 6359-6411 (2023).

7 Olsbye, U. *et al.* Conversion of Methanol to Hydrocarbons: How Zeolite Cavity and Pore Size Controls Product Selectivity. *Angew. Chem. Int. Ed.* **51**, 5810-5831 (2012).

8 Olah, G. A. Towards Oil Independence Through Renewable Methanol Chemistry. *Angew. Chem. Int. Ed.* **52**, 104-107 (2013).

9 Lu, K. *et al.* High Ethylene Selectivity in Methanol-to-Olefin (MTO) Reaction over MOR-Zeolite Nanosheets. *Angew. Chem. Int. Ed.* **59**, 6258-6262 (2020).

10 Kamat, P. V. & Jin, S. Semiconductor Photocatalysis: "Tell Us the Complete Story!". *ACS Energy Lett.* **3**, 622-623 (2018).

11 Qi, M.-Y., Conte, M., Anpo, M., Tang, Z.-R. & Xu, Y.-J. Cooperative coupling of oxidative organic synthesis and hydrogen production over semiconductor-based photocatalysts. *Chem. Rev.* **121**, 13051-13085 (2021).

12 Chen, X., Shen, S., Guo, L. & Mao, S. S. Semiconductor-based Photocatalytic Hydrogen Generation. *Chem. Rev.* **110**, 6503-6570 (2010).

13 Cheng, J.-K. & Loh, T.-P. Copper- and Cobalt-Catalyzed Direct Coupling of sp^3 α-Carbon of Alcohols with Alkenes and Hydroperoxides. *J. Am. Chem. Soc.* **137**, 42-45 (2015).

14 Zhang, S.-Y., Zhang, F.-M. & Tu, Y.-Q. Direct Sp^3 α-C–H activation and functionalization of alcohol and ether. *Chem. Soc. Rev.* **40**, 1937-1949 (2011).

15 Qi, M.-Y., Li, Y.-H., Anpo, M., Tang, Z.-R. & Xu, Y.-J. Efficient Photoredox-Mediated C-C Coupling Organic Synthesis and Hydrogen Production over Engineered Semiconductor Quantum Dots. *ACS Catal.* **10**, 14327-14335 (2020).

16 Peng, Y. *et al.* Photocatalytic synthesis of ethylene glycol and hydrogen from methyl tert-butyl ether. *Nat. Commun.* **16**, 3959 (2025).

17 Wang, L. *et al.* Precisely Constructed Metal Sulfides with Localized Single-Atom Rhodium for Photocatalytic C−H Activation and Direct Methanol Coupling to Ethylene Glycol. *Adv. Mater.* **35**, 2205782 (2023).

18 Luo, N. *et al.* Low-Work Function Metals Boost Selective and Fast Scission of Methanol C–H Bonds. *ACS Catal.* **12**, 6375-6384 (2022).

19 Zhang, H. *et al.* C-H activations of methanol and ethanol and C-C couplings into diols by zinc-indium-sulfide under visible light. *Chem. Commun.* **56**, 1776-1779 (2020).

20 Wang, L. *et al.* Solar energy-driven C−H activation of methanol for direct C−C coupling to ethylene glycol with high stability by nitrogen doped tantalum oxide. *Chin. J. Catal.* **42**, 1459-1467 (2021).

21 Liang, J. *et al.* Oxygen-Activated Boron Nitride for Selective Photocatalytic Coupling of Methanol to Ethylene Glycol. *Angew. Chem. Int. Ed.* **63**, e202318236 (2024).

22 Luo, J. *et al.* Photocatalytic Methanol Dehydrogenation with Switchable Selectivity. *J. Am. Chem. Soc.* **147**, 3428-3437 (2025).

23 Faveere, W. H. *et al.* Toward Replacing Ethylene Oxide in a Sustainable World: Glycolaldehyde as a Bio-Based C_2 Platform Molecule. *Angew. Chem. Int. Ed.* **60**, 12204-12223 (2021).

24 Garrabou, X. *et al.* Asymmetric Self- and Cross-Aldol Reactions of Glycolaldehyde Catalyzed by D-Fructose-6-phosphate Aldolase. *Angew. Chem. Int. Ed.* **48**, 5521-5525 (2009).

25 Powner, M. W., Zheng, S.-L. & Szostak, J. W. Multicomponent Assembly of Proposed DNA Precursors in Water. *J. Am. Chem. Soc.* **134**, 13889-13895 (2012).

26 Faveere, W. *et al.* Glycolaldehyde as a Bio-Based C_2 Platform Chemical: Catalytic Reductive Amination of Vicinal Hydroxyl Aldehydes. *ACS Catal.* **10**, 391-404 (2020).

27 Zhang, N. *et al.* Near-field dielectric scattering promotes optical absorption by platinum nanoparticles. *Nat. Photonics* **10**, 473-482 (2016).

28 Qi, M.-Y. & Xu, Y.-J. Efficient and Direct Functionalization of Allylic sp^3 C−H Bonds with Concomitant CO_2 Reduction. *Angew. Chem. Int. Ed.* **62**, e202311731 (2023).

29 Qi, M.-Y., Conte, M., Tang, Z.-R. & Xu, Y.-J. Engineering semiconductor quantum dots for selectivity switch on high-performance heterogeneous coupling photosynthesis. *ACS Nano* **16**, 17444-17453 (2022).

30 Zang, W. *et al.* Efficient hydrogen evolution of oxidized Ni-N_3 defective sites for alkaline freshwater and seawater electrolysis. *Adv. Mater.* **33**, 2003846 (2021).

31 Lin, L. *et al.* Atomically dispersed Ni/alpha-MoC catalyst for hydrogen production from methanol/water. *J. Am. Chem. Soc.* **143**, 309-317 (2021).

32 Xia, C. *et al.* General synthesis of single-atom catalysts with high metal loading using graphene quantum dots. *Nat. Chem.* **13**, 887-894 (2021).

33 Qian, G. *et al.* Efficient photoreduction of diluted CO_2 to tunable syngas by Ni-Co dual sites through d-band center manipulation. *Angew. Chem. Int. Ed.* **61**, e202210576 (2022).

34 Denisov, N. *et al.* Light-Induced Agglomeration of Single-Atom Platinum in Photocatalysis. *Adv. Mater.* **35**, 2206569 (2023).

35 Sarma, B. B., Maurer, F., Doronkin, D. E. & Grunwaldt, J.-D. Design of Single-Atom Catalysts and Tracking Their Fate Using Operando and Advanced X-ray Spectroscopic Tools. *Chem. Rev.* **123**, 379-444 (2023).

36 Yang, J., Wang, D., Han, H. & Li, C. Roles of Cocatalysts in Photocatalysis and Photoelectrocatalysis. *Acc. Chem. Res.* **46**, 1900-1909 (2013).

37 Li, X., Yu, J., Jaroniec, M. & Chen, X. Cocatalysts for selective photoreduction of CO_2 into solar fuels. *Chem. Rev.* **119**, 3962-4179 (2019).

38 Yan, X. *et al.* An electron-hole rich dual-site nickel catalyst for efficient photocatalytic overall water splitting. *Nat. Commun.* **14**, 1741 (2023).

39 Lu, Q. *et al.* One-pot synthesis of interconnected $Pt_{95}Co_5$ nanowires with enhanced electrocatalytic performance for methanol oxidation reaction. *Nano Res.* **11**, 2562-2572 (2018).

40 Kakati, N. *et al.* Anode Catalysts for Direct Methanol Fuel Cells in Acidic Media: Do We Have Any Alternative for Pt or Pt–Ru? *Chem. Rev.* **114**, 12397-12429 (2014).

41 Liu, J. *et al.* Designing Nanoporous Coral-Like Pt Nanowires Architecture for Methanol and Ammonia Oxidation Reactions. *Adv. Funct. Mater.* **32**, 2110702 (2022).

42 Fan, Y. *et al.* Photocatalytic Coupling of Methanol and Formaldehyde into Ethylene Glycol with High Atomic Efficiency. *Catal. Lett.* **148**, 2274-2282 (2018).

43 Blöchl, P. E. Projector augmented-wave method. *Phys. Rev. B* **50**, 17953-17979 (1994).

44 Perdew, J. P. *et al.* Atoms, molecules, solids, and surfaces: Applications of the generalized gradient approximation for exchange and correlation. *Phys. Rev. B* **46**, 6671-6687 (1992).

Acknowledgements

This work was supported by the National Natural Science Foundation of China (22572017 and 22072023 to Z.-R.T.; 22472032 and 22172030 to Y.-J.X.), the Program for National Science and Technology Innovation Leading Talents (00387072 to Y.-J.X.), the Research Fund for Outstanding Talents at University of Electronic Science and Technology of China (A1098531023601522 to Y.-J.X.), the China Postdoctoral Science Foundation (2023M740513 to M.-Y.Q.), the China National Postdoctoral Program for Innovative Talents (BX20240055 to M.-Y.Q.), the Jiangxi Province "Double Thousand Plan" (No. jxsq2023102143 to Y.-J.X.) and the Natural Science Foundation of Sichuan Province (2026NSFSC0077 to Y.-J.X.; 2026NSFSC0078 to Z.-R.T.; 2026NSFSC0831 to M.-Y.Q.).

Author contributions

M.-Y.Q. and Y.-J.X. created the concept and designed the overall project. M.-Y.Q. designed and conducted the experiments, analyzed the data and drafted the article. C.-L.T., Z.-R.T., M.C. and Y.S reviewed and edited the manuscript. All the authors discussed and revised the paper.

Competing interests

The authors declare no competing financial interests.

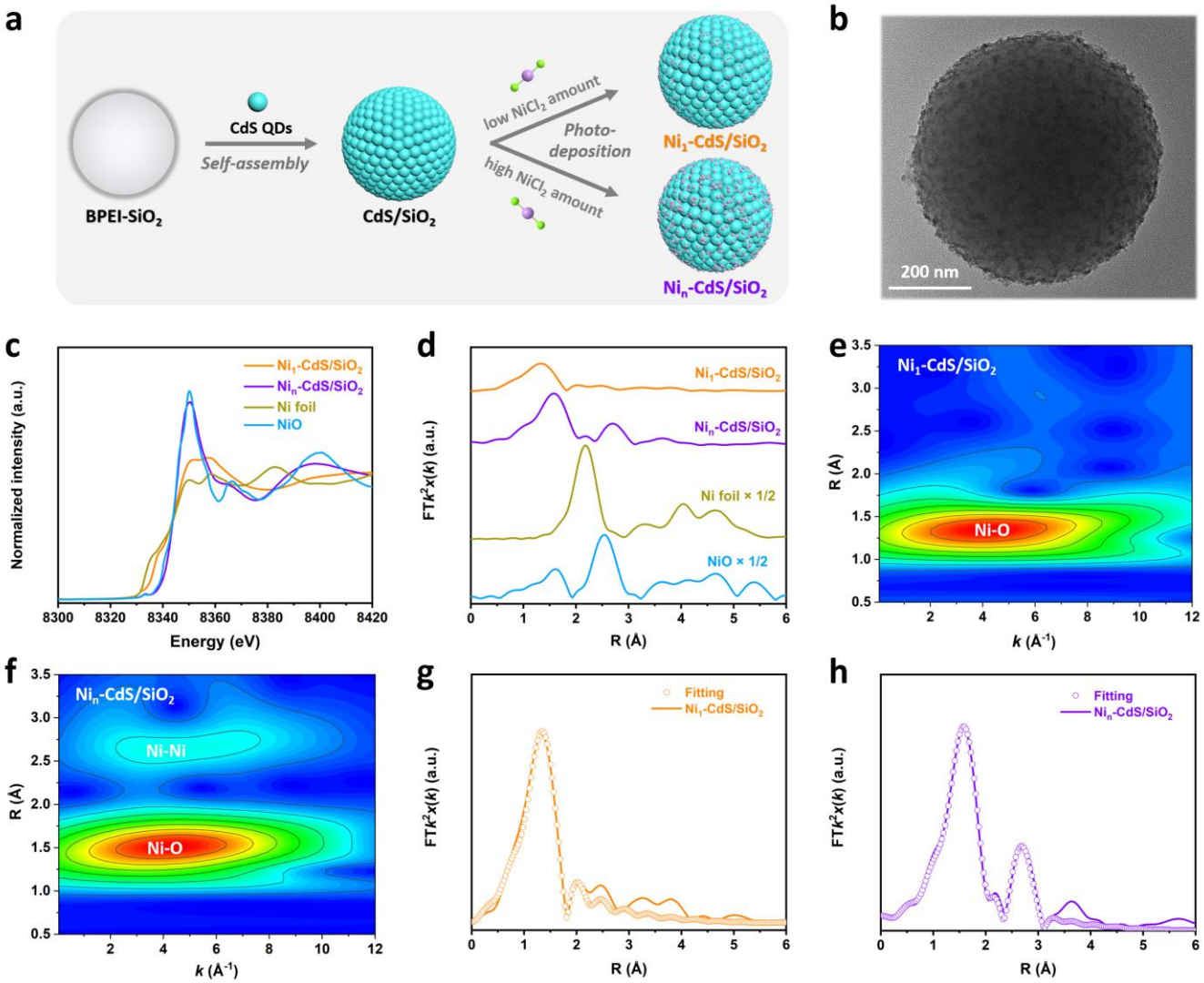

Fig. 1 | Preparation and characterization of Ni-CdS/SiO_2 with atomically dispersed Ni species. **a**, Synthesis procedure for the Ni-CdS/SiO_2 composite. **b**, TEM image of CdS/SiO_2 composite, **c**,**d** Normalized Ni K-edge XANES spectra (**c**) and FT-EXAFS spectra (**d**) of Ni-CdS/SiO_2 along with Ni foil and NiO as references. Wavelet transform for Ni K-edge EXAFS spectra of (**e**) Ni_1-CdS/SiO_2 and (**f**) Ni_n-CdS/SiO_2. **g**,**h**, EXAFS fitting curves for (**g**) Ni_1-CdS/SiO_2 with single Ni atoms and (**h**) Ni_n-CdS/SiO_2 with Ni clusters.

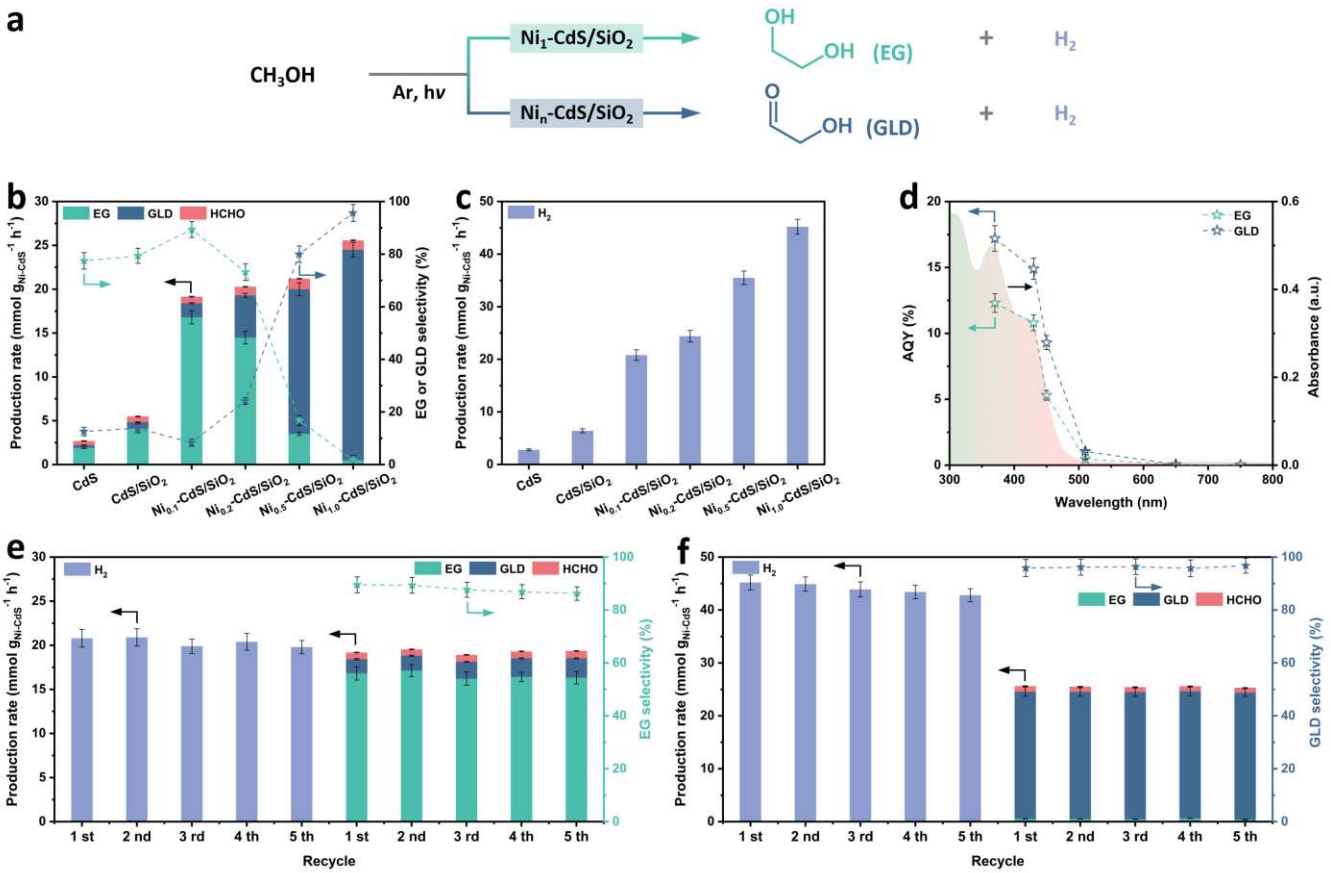

Fig. 2 | Selective switchable dehydrocoupling of methanol to produce EG or GLD. a, Schematic representation of the chemical reactions for conversion of methanol into EG or GLD as well as H_2. **b**, Production rate of various products and EG or GLD selectivity over CdS, CdS/SiO_2 and Ni-CdS/SiO_2 composites with different Ni loading amounts. **c**, H_2 production rate over CdS, CdS/SiO_2 and Ni-CdS/SiO_2 composites with different Ni loading amounts. Standard conditions: 20 mg catalyst in 10 mL of methanol solution, Ar atmosphere, 300 W xenon lamp, 10 h, room temperature. **d**, Diffuse reflectance spectroscopy (DRS) spectrum of CdS/SiO_2 composite and AQYs for EG or GLD production over Ni-CdS/SiO_2 composite under different monochromatic lights. **e**,**f**, Recycling performance of (**e**) Ni_1-CdS/SiO_2 composite with single Ni atoms and (**f**) Ni_n-CdS/SiO_2 composite with Ni clusters. Error bars represent the standard deviation derived from three independent measurements. The arrow symbols in the **Fig. 2b, d-f** represent the direction to the corresponding vertical coordinates.

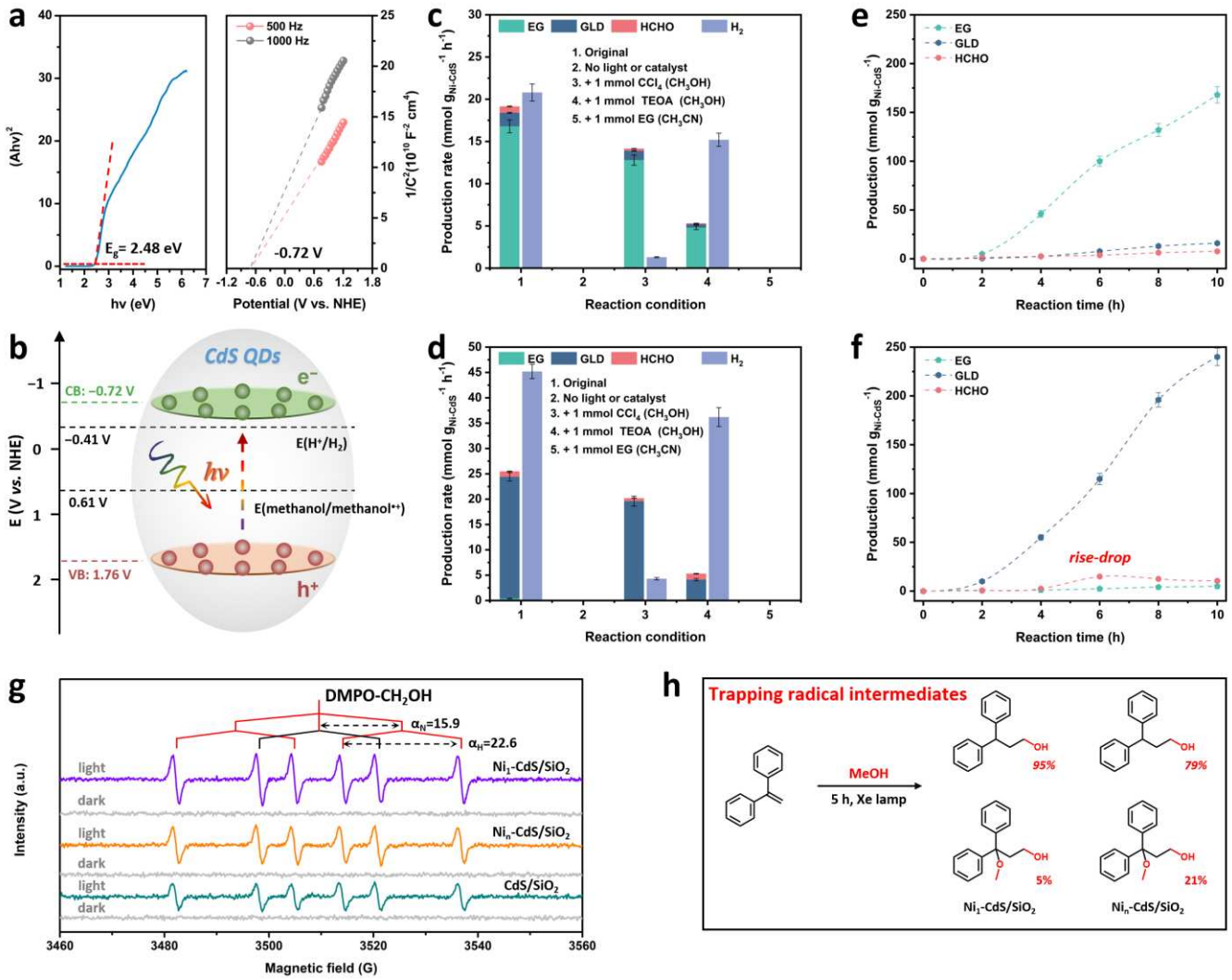

Fig. 3 | Mechanism insight for dehydrocoupling of methanol. **a**, Tauc plot (left) and Mott-Schottky plots (right) for CdS QDs. **b**, Redox potentials of methanol oxidation and H_2 evolution against the VB and CB edges of CdS QDs. **c**,**d**, Control experiments with different additives catalyzed by (**c**) Ni_1-CdS/SiO_2 and (**d**) Ni_n-CdS/SiO_2 composite. Standard conditions: 20 mg catalyst in 10 mL of CH_3OH (entries 1-4) or CH_3CN solution (entry 5), Ar atmosphere, 300 W xenon lamp, 10 h, room temperature. Error bars represent the standard deviation derived from three independent measurements. **e**,**f**, Time profiles of products evolution over (**e**) Ni_1-CdS/SiO_2 and (**f**) Ni_n-CdS/SiO_2 composite. **g**, In-situ EPR spectra of CdS/SiO_2, Ni_1-CdS/SiO_2 and Ni_n-CdS/SiO_2 composite in Ar saturated methanol solution in the presence of DMPO. **h**, Capturing radical intermediates by DPE in dehydrocoupling of methanol. Standard conditions: 20 mg catalyst in 10 mL of CH_3OH solution with 1 mmol of 1,1-diphenylethylene, Ar atmosphere, 300 W xenon lamp, 5 h, room temperature.

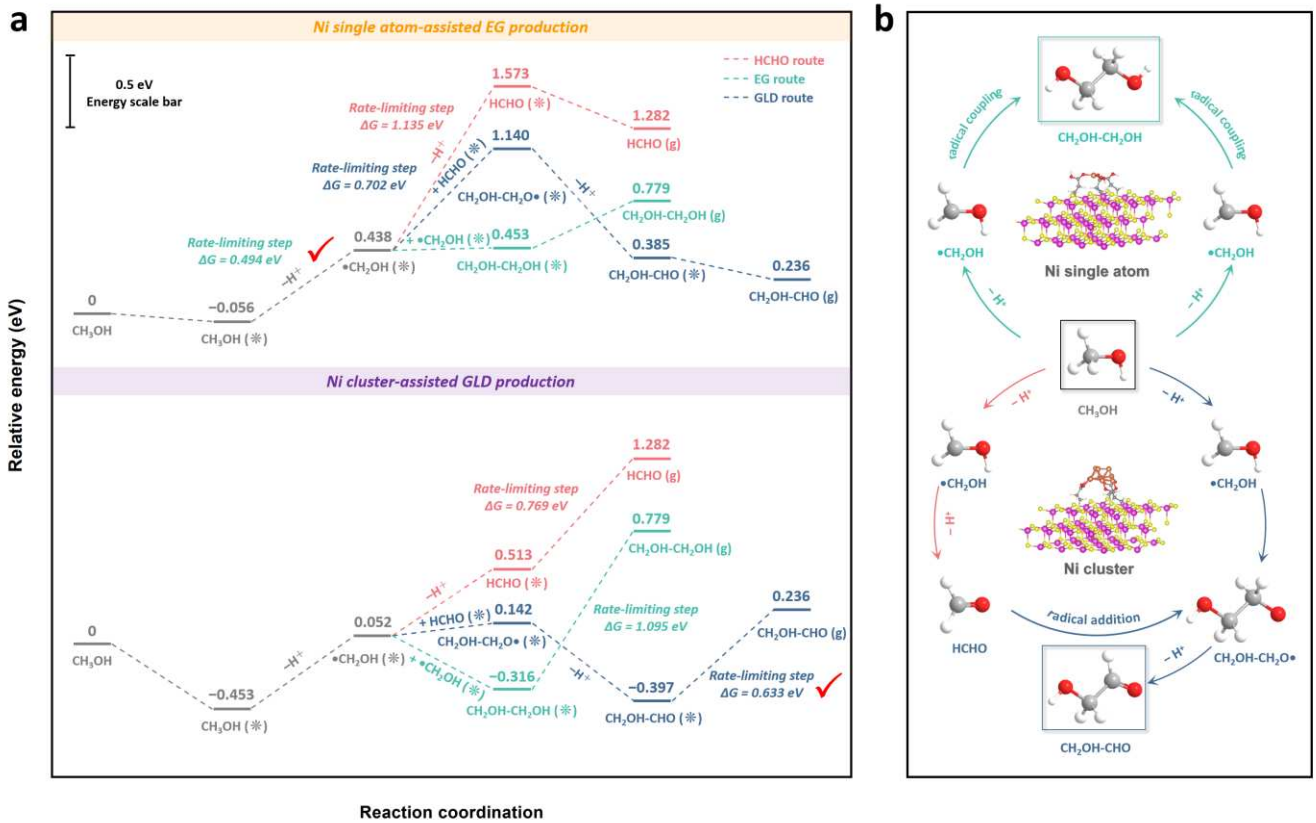

Fig. 4 | DFT calculations and proposed mechanism. a, Calculated potential energy diagrams for dehydrocoupling of methanol catalyzed by Ni single atoms in Ni_1-CdS and Ni clusters in Ni_n-CdS, respectively (via bonding with the O atom in CH_3OH/intermediates). **b**, Proposed mechanism for switchable methanol C−C coupling to EG or GLD. Atoms in brown, red, pink, yellow, grey and white represent Ni, O, Cd, S, C and H respectively.

Editorial Summary

This study tailors atomically dispersed Ni species on SiO_2-supported CdS quantum dots to enable efficient photoredox-driven C−C coupling of methanol for divergent synthesis of high-value C_2 chemicals with concomitant H_2 production.

Peer Review Information: *Nature Communications t*hanks the anonymous, reviewer(s) for their contribution to the peer review of this work. A peer review file is available."